Enhanced spin-polarization via partial Ge-dimerization as the driving force of the charge density wave in FeGe

Yilin Wang *

School of Emerging Technology, University of Science and Technology of China, Hefei, Anhui 230026, China

(Received 10 April 2023; accepted 16 October 2023; published 30 October 2023)

A $2 \times 2 \times 2$ charge density wave (CDW) was recently observed deep inside the antiferromagnetic phase of a kagome metal FeGe, which significantly enhances its spin-polarization. A key question is whether the CDW in FeGe is driven by its electronic correlation and magnetism. Here, we address this problem using density functional theory and its combination with U as well as dynamical mean-field theory. Our calculations show that large dimerization ($\sim$1.3 Å) of Ge1 sites along the c axis will enhance electronic correlation of the Fe-3d orbitals and, as a result, it enhances the spin-polarization and saves more magnetic exchange energies. We find that the balance between magnetic energy saving and structural energy cost via partially dimerizing Ge1 sites in an enlarged superstructure could induce a new local minimum in total energies. The response to the large partial Ge1-dimerization will induce additional small modulations ($<$0.05 Å) of other sites in the kagome and honeycomb layers, which further reduces the total energy and leads to a stable $2 \times 2 \times 2$ CDW ground state in FeGe. Our results are in good agreement with the existing experiments and reveal a different unconventional CDW mechanism driven by primarily saving magnetic energies via the interplay of structure, electronic correlation, and magnetism.

DOI: 10.1103/PhysRevMaterials.7.104006

I. INTRODUCTION

A charge density wave (CDW), the static modulations of small amplitude in the electron density distribution accompanied by a periodic lattice distortion [1,2], is one of the most important phases of matter in condensed matter physics. A common driving force for a CDW includes Fermi-surface nesting [3] and electron-phonon couplings [4–7]. A more exotic mechanism driven by strong electron-electron interactions is also suggested, for example, in copper oxides [8–16] and nickel oxides [17,18]. Recently, an exotic chiral $2 \times 2 \times 2$ CDW that breaks time-reversal symmetry was observed [19,20] in a kagome metal AV_3Sb_5 (A=K, Rb, Cs) [21–23], which was suggested to be triggered by van Hove singularities (VHSs) [24–35]. Since kagome metals can simultaneously feature geometry frustration [36–38], flat-band-induced electronic correlation [39–44] and magnetism [45–50], nontrivial topology [22,51–53], VHSs [25,26], as well as strong electron-phonon interactions [54–57], it has become an ideal platform for exploring CDWs driven by various mechanisms.

Very recently, another $2 \times 2 \times 2$ CDW was observed around $T_{CDW} = 100$ K, deep inside the A-type antiferromagnetic (AFM) phase ($T_N \sim 410$ K) of a magnetic kagome metal FeGe [59,60]. Both neutron [59] and x-ray [61] scattering experiments indicate a first-order nature of this CDW transition. Possible anomalous Hall effect [59] and topological edge modes [60] were observed in its CDW phase, which are similar to those observed in AV_3Sb_5 [23,62]. However, there are more differences between the CDWs in FeGe and AV_3Sb_5. (i) The ordered magnetic moments were found to be enhanced in the CDW phase of FeGe [59]. (ii) A sharp superlattice peak, $Q = (0, 0, 2.5)$, that probes lattice distortion along the c axis was observed in FeGe by the x-ray scattering experiment with the same onset temperature as CDW [61], which is absent in AV_3Sb_5. (iii) First-principles calculations find only a little phonon softening around the three L points, i.e., (0.5, 0, 0.5), (0, 0.5, 0.5), and (−0.5, 0.5, 0.5), but the phonon frequencies never become negative in FeGe in the parameter regime that produces the correct ordered magnetic moment [61]. Such behavior in the phonon spectrum is very different from AV_3Sb_5 [27,54], while it shows some similarities to the electronic-correlation-driven CDWs in copper and nickel oxides. These indicate a different origin of the CDW in FeGe, in sharp contrast to AV_3Sb_5. A natural question thus arises as to whether the CDW in FeGe is driven by its electronic correlation and magnetism. Despite several investigations by experiment [59–61,63] and theoretical calculations [61,64–68], the driving force of the CDW in FeGe still remains an open question.

In a previous work [61] that primarily focuses on the phonon properties of FeGe, we have obtained a stable $2 \times 2 \times 2$ superstructure of FeGe with lower energy than its ideal structure by density functional theory (DFT) calculation, guided by the soft phonon mode at L points and the first-order nature of the CDW transition in FeGe. A key finding is that there is a large dimerization ($\sim$1.3 Å) of 1/4 of Ge1 sites along the c axis in the $2 \times 2 \times 2$ superstructure. However, based on the information in [61], a clear physical picture on *exactly how the interplay of electronic correlations, magnetism, and lattice drives the CDW in FeGe* is still unknown.

*yilinwang@ustc.edu.cn

To be specific, (i) What drives such a large Ge1-dimerization and why is it stable? (ii) Why is the large Ge1-dimerization partial (1/4), not full? (iii) Why is a $2 \times 2 \times 2$ superstructure, and not another superstructure, chosen as the ground state? (iv) Since there are also small distortions of the Fe and Ge2 sites, which distortions drive the enhancement of spin-polarization, and how? (v) Which energies are primarily saved in forming the CDW: electronic, magnetic, or structural?

In this work, we focus on answering these questions to identify the driving force for the CDW in FeGe, using DFT and its combination with U (DFT+U) as well as dynamical mean-field theory (DFT+DMFT) [69,70]. Our calculations show that large dimerization of Ge1 sites along the c axis will enhance electronic correlation of the Fe-3d orbitals and, as a result, enhance the spin-polarization and save more magnetic exchange energies. We find that the balance between magnetic energy saving and structural energy cost via partially dimerizing Ge1 sites in an enlarged superstructure could induce a new local minimum in total energies. The response to the large partial Ge1-dimerization will induce additional small modulations (<0.05 Å) of other sites in the kagome and honeycomb layers, which further reduces the total energy and leads to a stable $2 \times 2 \times 2$ CDW ground state in FeGe. Thus, our results demonstrate a clear physical picture for the CDW formation in FeGe and reveal an unconventional CDW mechanism driven primarily by saving magnetic energies via the interplay of structure, electronic correlation, and magnetism, which are in good agreement with the existing experiments.

II. METHODS

As shown in Fig. 1(a), hexagonal FeGe consists of a kagome layer of Fe_3Ge and a honeycomb layer of Ge_2. There are two nonequivalent Ge sites: Ge1 (blue) in the center of the hexagon of the Fe kagome structure and Ge2 (gray) in the honeycomb layer. The DFT calculations are performed using the VASP package [71,72], with the exchange-correlation functional of the generalized gradient approximation (GGA) [73]. Although FeGe is a strongly correlated magnet, the DFT calculations without Hubbard U correction have already correctly produced the ordered magnetic moments of its AFM phase (around 1.5 μ_B/Fe), observed by a neutron scattering experiment [59]. Therefore, DFT calculations are applicable to the AFM phase of FeGe. The experimental lattice parameters of FeGe, $a = 4.985$ Å and $c = 4.048$ Å [59,74], are used in the calculations.

To better capture the strong electronic correlations of FeGe, we also perform fully charge self-consistent single-site DFT+DMFT calculations for its paramagnetic (PM) and AFM phases, using the EDMFTF code developed by Haule *et al.* [75,76] based on the WIEN2K package [77]. For the AFM calculation, a nonmagnetic calculation is performed in the DFT part, while the AFM spin-polarization is considered in the DMFT part by breaking the spin degeneracy of the local self-energy. The Hubbard U and Hund's coupling J_H are chosen to be 3.9 and 0.85 eV, respectively, to reproduce the ordered magnetic moments that are observed experimentally. We note that a larger U value is required on the dynamical mean-field level than the static mean-field level in DFT+U to produce the same ordered magnetic moments. This is reasonable since local spin fluctuations are considered in DFT+DMFT, but not in DFT+U. More computational details are presented in Appendix A.

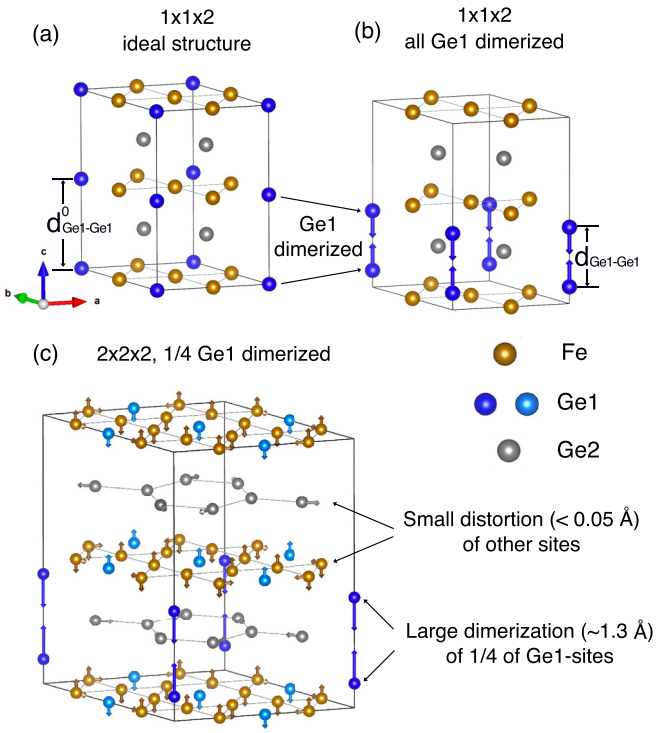

FIG. 1. (a) $1 \times 1 \times 2$ ideal kagome structure of FeGe. There are two types of Ge sites. Ge1 (dark blue) is at the center of the hexagon of the Fe kagome layer. Ge2 (gray) forms a honeycomb layer in between two kagome layers. (b) All the Ge1 atoms deviate from the kagome layers and form dimers along the c axis. The strength of Ge1 dimerization is defined as $d = d^0_{\text{Ge1-Ge1}} - d_{\text{Ge1-Ge1}}$, where $d^0_{\text{Ge1-Ge1}}$ and $d_{\text{Ge1-Ge1}}$ are the bond lengths of Ge1-Ge1 before and after dimerization, respectively. (c) A $2 \times 2 \times 2$ superstructure of FeGe with space group $P6/mmm$. It consists of a large dimerization ($|d| \sim 1.3$ Å) of 1/4 of the Ge1 sites along the c axis and small distortion (<0.05 Å, indicated by short arrows) of other sites. The Ge1-Ge1 bond lengths before and after dimerization are 4.0 and 2.755 Å, respectively. The crystal structures are constructed using VESTA [58].

III. RESULTS

Figure 2 shows the results calculated by DFT. Figure 2(a) shows the total energy difference of the $1 \times 1 \times 2$ superstructure of FeGe between the one with large dimerization of all the Ge1 sites along the c axis and the one without dimerization, $\Delta E = E_{\text{tot}}(d) - E_{\text{tot}}(d = 0)$, as functions of the Ge1-dimerization strength d (see Fig. 1). ΔE for the nonmagnetic (NM) state keeps increasing with $|d|$, indicating that it has to pay for energies for structure distortions. However, the increasing rate slows down when the dimerization strength d is ~1.0–1.3 Å. When $d = 1.3$ Å, the Ge1-Ge1 bond lengths before and after dimerization are 4.0 and 2.755 Å, respectively. We note that 2.755 Å is close to the Ge-Ge bond length (~2.5 Å) in the diamond cubic crystal structure of Ge. Therefore, Ge1 atoms are easier to form dimers when their bond lengths are close to this value. Although ΔE

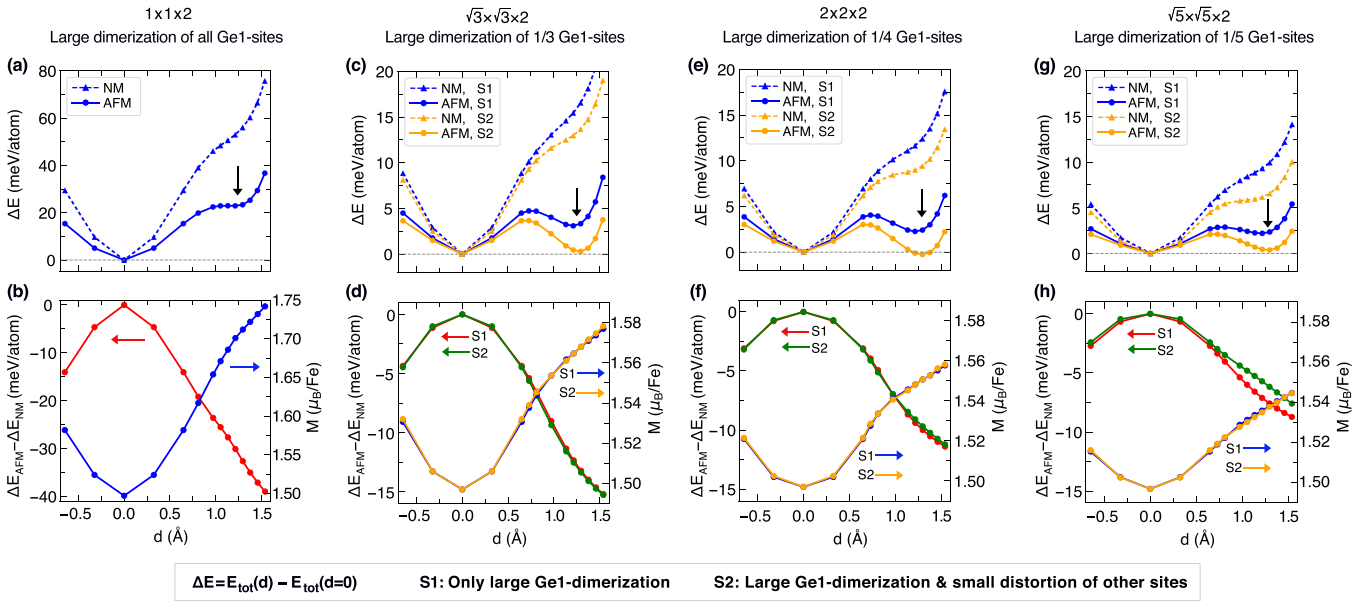

FIG. 2. Enhanced spin-polarization via partial Ge1-dimerization calculated by DFT. (a) The difference of total energy between the distorted and ideal kagome structure, $\Delta E = E_{\rm tot}(d) - E_{\rm tot}(d=0)$, as functions of the strength of Ge1-dimerization d. Dashed and solid curves are for nonmagnetic and antiferromagnetic states, respectively. The black arrow labels a local energy minimum around $d = 1.3$ Å. (b) The magnetic exchange energy, $\Delta E_{\rm AFM} - \Delta E_{\rm NM}$, and the average of ordered magnetic moments per Fe in the AFM state as functions of d are shown in the left and right y axis, respectively. (a) and (b) are for the $1 \times 1 \times 2$ structure with large dimerization of all Ge1 sites. (c)–(h) are analogous to (a) and (b), but for enlarged superstructures and two different cases labeled "S1" and "S2" (see the main text). (c) and (d) are for the $\sqrt{3} \times \sqrt{3} \times 2$ superstructure ($P6/mmm$) with large dimerization of 1/3 of Ge1 sites. (e) and (f) are for the $2 \times 2 \times 2$ superstructure ($P6/mmm$) with large dimerization of 1/4 of Ge1 sites. (g) and (h) are for the $\sqrt{5} \times \sqrt{5} \times 2$ superstructure ($Cmmm$) with large dimerization of 1/5 of Ge1 sites.

also increases with $|d|$ for the AFM state, its magnitude is much smaller than that of the NM state, indicating that the spin-polarization is enhanced and more magnetic exchange energies are saved by Ge1-dimerization. This is shown in Fig. 2(b), where the magnetic exchange energies, $\Delta E_{\rm AFM} - \Delta E_{\rm NM}$, are negative and their magnitude keeps increasing with $|d|$ (left y axis), and the ordered magnetic moments also increase with $|d|$ (right y axis). This is a main finding of the present work. The competition between magnetic energy saving from enhanced spin-polarization and structural energy cost from Ge1-dimerization may induce a new local minimum in the total energies of the AFM state, as illustrated by the black arrow around $d = 1.3$ Å in Fig. 2(a). It may further become a global energy minimum if the magnetic energy wins and drive a first-order phase transition. This has not been achieved in the $1 \times 1 \times 2$ superstructure because it costs too much structural energy to dimerize all the Ge1 sites. Therefore, a straightforward strategy to balance the magnetic energy saving and structural energy cost is to enlarge the structure along the a and b crystal axis, but dimerize partial Ge1 sites.

Along this line, we construct three superstructures: $\sqrt{3} \times \sqrt{3} \times 2$ with large dimerization of 1/3 of Ge1 sites [Figs. 2(c) and 2(d)], $2 \times 2 \times 2$ with large dimerization of 1/4 of Ge1 sites [Figs. 2(e) and 2(f)], and $\sqrt{5} \times \sqrt{5} \times 2$ with large dimerization of 1/5 of Ge1 sites [Figs. 2(g) and 2(h)]. We then perform calculations for two different cases: (S1) The superstructure with only fixed large dimerization of partial Ge1 sites but other sites are not relaxed; (S2) the superstructure with fixed large dimerization of partial Ge1 sites and all the other sites are relaxed until the force of each of those atoms is less than 1 meV/Å.

As shown by the solid blue curves in Figs. 2(c), 2(e), and 2(g), well-defined local energy minimums have already formed around $d = 1.3$ Å in all three superstructures with only large partial Ge1-dimerization (S1). The energy minimums are only ∼2–3 meV/atoms higher than that of the non-distorted structures ($d = 0$). The magnetic exchange energies and the ordered magnetic moments shown in Figs. 2(d), 2(f), and 2(h) follow the same behaviors as the $1 \times 1 \times 2$ superstructure. Large dimerization of partial Ge1 sites will exert extra potential on other sites, such that they will slightly relax their positions to further reduce the total energy, which are shown by the solid orange curves in Figs. 2(c), 2(e), and 2(g). The energy minimums around $d = 1.3$ Å of all three superstructures get much closer to that of the ideal structure, but it only becomes a global minimum in the $2 \times 2 \times 2$ superstructure, consistent with the experimentally observed $2 \times 2 \times 2$ CDW in FeGe. This is because the 1/3 Ge1-dimerization in the $\sqrt{3} \times \sqrt{3} \times 2$ superstructure pays for more structural distortion energy and the 1/5 Ge1-dimerization in the $\sqrt{5} \times \sqrt{5} \times 2$ superstructure cannot save enough magnetic energy, comparing to the 1/4 Ge1-dimerization in the $2 \times 2 \times 2$ superstructure. Therefore, we can conclude that the form of the $2 \times 2 \times 2$ CDW superstructure in FeGe results from a subtle balance between magnetic exchange energy saving and structure energy cost via large structural dimerization of 1/4 of Ge1 sites.

TABLE I. The mass enhancement, $m^*/m^{\mathrm{DFT}} = 1/Z$, of Fe-3$d$ orbitals from DFT+DMFT calculations of the paramagnetic phase of the $1 \times 1 \times 2$ superstructure with ($d = 1.3$ Å) and without ($d = 0$ Å) Ge1-dimerization, at $T = 290$ K, $U = 3.9$ eV, and $J_H = 0.85$ eV.

	$d_{3z^2-r^2}$	$d_{x^2-y^2}$	d_{xz}	d_{yz}	d_{xy}
$d = 0$ Å	2.146	3.232	3.342	3.239	2.055
$d = 1.3$ Å	2.287	3.971	4.171	3.642	2.136

The distortions of other sites are very small (<0.05 Å). The arrows in Fig. 1(c) illustrate such distortions in the $2 \times 2 \times 2$ superstructure. In the kagome layers, the atoms mainly move out of plane along the c axis, and with a small in-plane component. In the honeycomb layers, the atoms move in plane to form a Kekulé-type distortion [65,78]. We note that the magnetic exchange energies and ordered magnetic moments are not further enhanced by those additional distortions [green curves in Figs. 2(d), 2(f), and 2(h)], indicating that the driving force for the enhanced spin-polarization is primarily from the large dimerization of Ge1 sites. The small 2×2 charge modulations in the kagome and honeycomb layers which are observed by the scanning tunneling microscopy (STM) experiments [59,60,79], are induced, as a consequence, to respond to the extra potential induced by the large dimerization of partial Ge1 sites.

In order to understand how Ge1-dimerization will enhance the spin-polarization, we compare the electronic correlations of the paramagnetic state of the $1 \times 1 \times 2$ superstructure with and without Ge1-dimerization by DFT+DMFT calculations. The calculated mass enhancement $m^\star/m^{\mathrm{DFT}}$ of Fe-3d orbitals at $T = 290$ K, $U = 3.9$ eV, and $J_H = 0.85$ eV is tabulated in Table I, which qualitatively agrees with a previous DFT+DMFT calculation [80]. The mass enhancement, in particular, of $d_{x^2-y^2}$, d_{xz}, and d_{yz} orbitals, increases substantially from the ideal kagome structure to the structure with a Ge1-dimerization of $d = 1.3$ Å. It indicates that the height of Ge1 atoms relative to the Fe kagome plane will affect the electronic correlations of the Fe-3d orbitals. This is similar to the iron-based superconductors, where the electronic correlations of Fe-3d orbitals are found to be very sensitive to the heights of As or Se sites [81–83]. Stronger electronic correlations will enhance the spin-polarization of the AFM state of FeGe. Analogous to Fig. 2, we also perform DFT+DMFT calculations for the $2 \times 2 \times 2$ superstructure, which are shown in Fig. 3. Similar profiles of energy and ordered magnetic moments as functions of d are produced, and a global energy minimum is also found around $d = 1.3$ Å, which validates the findings from the simple DFT calculations.

The subtle competition between magnetic and structural energy indicates that the $2 \times 2 \times 2$ CDW in FeGe is sensitive to the variation of its magnetism and crystal structure. Thus, on the one hand, increasing Hubbard U in DFT+U calculations is expected to further save the magnetic energy and stabilize the CDW state. The DFT+U results at $U = 1$ eV for the $2 \times 2 \times 2$ superstructure are shown in Figs. 4(a) and 4(b). The ordered magnetic moment is enhanced to about 2 μ_B/Fe, much larger than the experimental value, and the energy of the CDW ground state is further reduced. We note that the energy minimum around $d = 1.3$ Å becomes a global

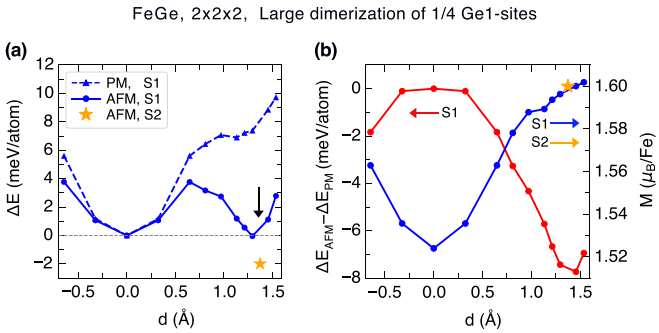

FIG. 3. Analogous to Fig. 2, but calculated by DFT+DMFT for paramagnetic (PM) and AFM phases of the $2 \times 2 \times 2$ superstructure, at $T = 290$ K, $U = 3.9$ eV, and $J_H = 0.85$ eV. Here, E stands for total free energy. The orange star in (a) and (b) stands for the total free energy and ordered magnetic moments, respectively, of the fully relaxed $2 \times 2 \times 2$ superstructure.

energy minimum even in the superstructure with only large dimerization of 1/4 of Ge1 sites (solid blue curve), which further confirms that the large dimerization of partial Ge1 sites is the driving force. We also find that the $\sqrt{3} \times \sqrt{3} \times 2$ superstructure becomes the ground state instead of the $2 \times 2 \times 2$ superstructure at $U = 1$ eV. This is also expected within our theory since the magnetic energy saving becomes even greater in the superstructure with more dimerized Ge1 sites at larger U, such that the $\sqrt{3} \times \sqrt{3} \times 2$ superstructure saves the most energy among the superstructures at $U = 1$ eV. This result further supports our conclusion that the CDW in FeGe results from a subtle competition between magnetic energy saving and structural energy cost.

On the other hand, elongating the crystal c axis of FeGe may cause it to pay for more structural distortion energy when dimerizing Ge1 sites. We show this in Figs. 4(c) and 4(d) by increasing c to 4.4 Å. Indeed, the $2 \times 2 \times 2$ CDW state is no longer favored.

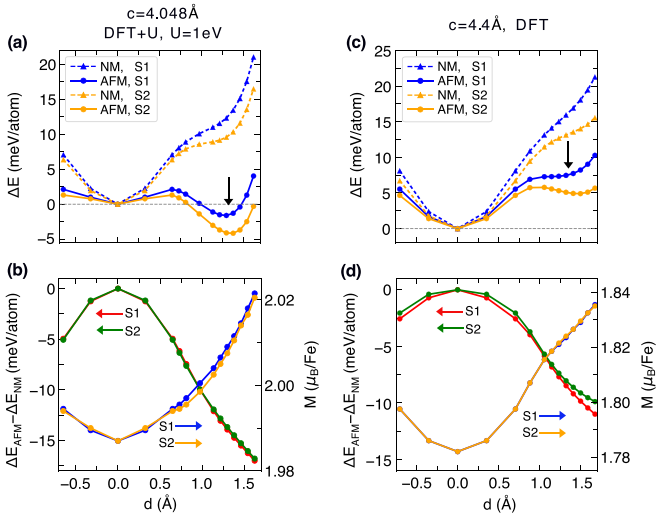

FIG. 4. Analogous to Fig. 2 for the $2 \times 2 \times 2$ superstructure of FeGe. (a) and (b) are calculated by DFT+U at $U = 1$ eV with the experimental lattice parameters. (c) and (d) are calculated by DFT, but with a larger lattice parameter of $c = 4.4$ Å.

IV. CONCLUSION AND DISCUSSION

To summarize, by DFT, DFT+U, and DFT+DMFT calculations, we show that the driving force of the $2 \times 2 \times 2$ CDW in FeGe is electronic-correlation-enhanced spin-polarization via large dimerization of partial Ge1 sites in an enlarged superstructure. The small 2×2 charge modulations in the kagome and honeycomb layers observed by STM [59,60,79] are thus induced as a consequence to respond to the large dimerization of partial Ge1 sites. We thus have established a clear physical picture for the CDW formation in FeGe and revealed an unconventional CDW mechanism driven primarily by saving magnetic energies via the interplay of electronic correlation, magnetism, and large lattice distortions.

Our results thus indicate a first-order CDW transition in FeGe, which is consistent with both neutron [59] and x-ray [61] scattering experiments. The large Ge1-dimerization along the c axis is consistent with the observation that an additional sharp superlattice peak $Q = (0, 0, 2.5)$ was found in the elastic x-ray scattering experiment with the same onset temperature as the CDW transition [61], since this peak probes the structural distortion along the c axis. The calculated enhancement of the ordered magnetic moments by 0.05 μ_B/Fe in the $2 \times 2 \times 2$ superstructure [Fig. 2(f)] is very close to the value observed by the neutron scattering experiment [59]. The enhancement of spin-polarization by electronic correlation should also be effective in the spin canting phase at $T = 60$ K and the spin-flop phase, so these two phases should not suppress CDW, which is also consistent with the phase diagram found in [59].

Similar to AV_3Sb_5, there are also VHSs at the M point near the Fermi level in the electronic structure of FeGe [59,61,63], so VHSs may also play roles in driving the CDW in FeGe. However, Wan *et al.* [67] have computed the nesting functions of FeGe and found that the maximum of the nesting function is at the K point instead of the M point. This excludes the possibility of VHSs or a Fermi-surface-nesting-induced CDW in FeGe.

We noted that although similar large Ge1-dimerization was also reported in Ref. [65] based on the DFT calculation, its crucial roles in enhancing the electronic correlations of Fe-3d orbitals and in driving the CDW in FeGe were not discussed. Instead, Ref. [65] suggests the Fermi-surface nesting as the driver of the CDW formation in FeGe. Thus, our DFT+DMFT calculations provide compelling evidence for the crucial role of electronic correlation effects related to the large Ge1-dimerization, in driving the CDW in FeGe, which has not been captured in previous investigations by the conventional DFT method.

ACKNOWLEDGMENTS

We thank Donglai Feng, Yajun Yan, Hu Miao, and Zhida Song for very helpful discussion. This project was supported by the National Natural Science Foundation of China (Grant No. 12174365). All the calculations were preformed on TianHe-1(A), the National Supercomputer Center in Tianjin, China.

Note added. Recently, the large 1/4 Ge1-dimerization has been confirmed by a recent single-crystal x-ray diffraction experiment [84] on a high-quality FeGe sample with long-range CDW order, which provides strong support for our present theoretical analysis.

Recently, an angle-resolved photoemission spectroscopy (ARPES) experiment [85] performed on the high-quality FeGe sample excludes the conventional Fermi-surface-nesting-induced CDW mechanism in FeGe, and instead provides strong support for the unconventional CDW mechanism proposed in the present work.

APPENDIX A: MORE COMPUTATIONAL DETAILS

In the VASP calculations, the energy cutoff of the plane-wave basis is set to be 500 eV. A Γ-centered K-point grid of $16 \times 16 \times 10$, $10 \times 10 \times 10$, $8 \times 8 \times 10$, and $6 \times 6 \times 10$ is used for the superstructures of $1 \times 1 \times 2$, $\sqrt{3} \times \sqrt{3} \times 2$, $2 \times 2 \times 2$, and $\sqrt{5} \times \sqrt{5} \times 2$, respectively. The criterion of total energy convergence is set to be 10^{-8} eV. For the case of S1, superstructures are construed by dimerizing one pair of Ge1 sites in adjacent layers along c axis, with a dimerization strength $d = d^0_{\text{Ge1-Ge1}} - d_{\text{Ge1-Ge1}}$, where $d^0_{\text{Ge1-Ge1}}$ and $d_{\text{Ge1-Ge1}}$ are the Ge1-Ge1 bond lengths before and after dimerization, respectively (see Fig. 1). For the case of S2, starting with the structures used in S1 and fixing the positions of the dimerized Ge1-Ge1 pair, the internal atomic positions of all other sites are relaxed until the force of each atom is smaller than 1 meV/Å (selective dynamics). For DFT+U calculations, the simplified (rotationally invariant) approach introduced by Dudarev *et al.* [86] is used (LDAUTYPE=2), which is parameterized by Hubbard U.

In DFT+DMFT calculations, the exchange-correlation functional of the local density approximation (LDA) is chosen in the DFT part. We choose a wide hybridization energy window from -10 to 10 eV with respect to the Fermi level. All five Fe-3d orbitals are considered as correlated ones and a local Coulomb interaction Hamiltonian with Ising form is applied. The local Anderson impurity model is solved by the continuous time quantum Monte Carlo solver [87]. We use a "nominal" double-counting scheme with a nominal Fe-3d occupancy of 6.0, which is close to the value given by the DFT calculation. The self-energy on real frequency $\Sigma(\omega)$ is obtained by the analytical continuation method of maximum entropy. The mass enhancement is then computed by $\frac{m^\star}{m^{\text{DFT}}} = 1 - \frac{\partial \text{Re}\Sigma(\omega)}{\partial \omega}|_{\omega=0}$. We follow the method introduced by Haule *et al.* [83] to perform structure relaxation in the framework of DFT+DMFT. All the calculations are performed at $T = 290$ K. Following Ref. [76], we use the Yukawa representation of the screened Coulomb interaction, in which there is a unique relationship between U and J_H. If U is specified, J_H is uniquely determined by a code in EDMFTF [88]. The U is chosen to be 3.9 eV, which correctly produces the ordered magnetic moment of the AFM phase of FeGe (about 1.5 μ_B/Fe). For AFM calculations, a constant self-energy which breaks the spin degeneracy is provided in the first step of DFT+DMFT self-consistency. For the WIEN2K calculations, a $12 \times 12 \times 13$ K-point grid is used for the $2 \times 2 \times 2$ superstructure. The radius of muffin-tin (RMT) values for Fe and Ge are 2.34 and 2.27, respectively, and $R_{\text{mt}} * K_{\text{max}}$ is 7.0. The spin-orbit coupling is not included in all the calculations

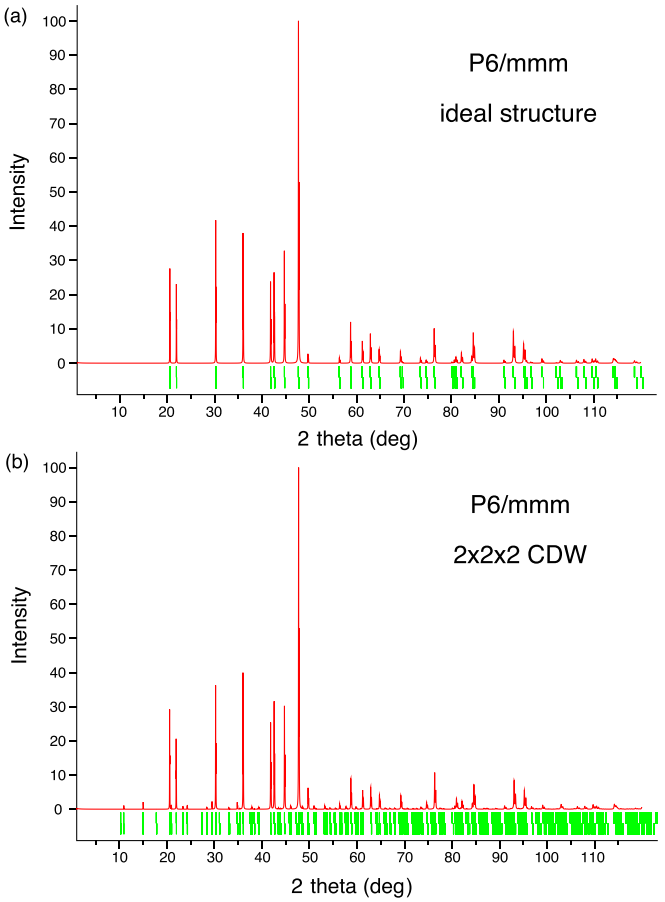

FIG. 5. Simulated XRD pattern of the (a) ideal structure and (b) $2 \times 2 \times 2$ CDW superstructure of FeGe.

since it is very small for the Fe and Ge ions and will not change the conclusions of the present work.

We note that a larger U value is required on the dynamical mean-field level than the static mean-field level in DFT+U to produce the same ordered magnetic moment. This is reasonable since the local spin fluctuations are considered in DFT+DMFT, but not in DFT+U. This is why the enhancement of the magnetic moment in DFT+DMFT at $U = 3.9$ eV and $J_H = 0.85$ eV (around 1.6) is lower than DFT+U at $U = 1$ eV (around 2); see the main text.

Due to a technical problem of the DFT+DMFT code used in this work, we cannot perform atomic relaxation in the *selective dynamics* mode as the VASP code does, i.e., it is difficult to fix the Ge1-Ge1 dimerization strength, but only relax other atoms. This is why we only show the result of the fully relaxed structure for the case (S2); see Fig. 3(a).

APPENDIX B: MORE RESULTS FOR FeGe

As shown in Fig. 5, we simulate the x-ray diffraction (XRD) pattern for the ideal structure and the distorted $2 \times 2 \times 2$ superstructure with large dimerization of 1/4 of the Ge1 site obtained in the main text, using the VESTA software [58]. Several additional reflection peaks with weak intensity appear in the $2 \times 2 \times 2$ superstructure, especially $2\theta \sim 10^\circ$ and 15°.

TABLE II. The atomic positions (fractional coordinates) of the $2 \times 2 \times 2$ CDW superstructure of FeGe relaxed by DFT. $a = 9.97$ Å, $c = 8.096$ Å, space group $P6/mmm$.

	x	y	z	Site	Sym.
Fe1	0.25182	0	0.75260	12n	..m
Fe2	0.24986	0.49972	0.74748	12o	.m.
Ge1	0	0	0.82990	2e	6mm
Ge2	0.5	0	0.74821	6i	2mm
Ge3	0.16919	0.33837	0	6l	mm2
Ge4	0.83796	0.67591	0.5	6m	mm2
Ge5	0.33333	0.66667	0	2c	$-6m$2
Ge6	0.33333	0.66667	0.5	2d	$-6m$2

We also tabulated the atomic positions of the $2 \times 2 \times 2$ CDW superstructure of FeGe in Table II.

We plot the charge density map of the $2 \times 2 \times 2$ CDW superstructure of FeGe in Fig. 6, which indeed shows the charge dimers of the 1/4 Ge1 sites.

To further confirm the stability of the $2 \times 2 \times 2$ CDW superstructure of FeGe with 1/4 of Ge1-dimerization, we have calculated the phonon spectra by DFT. As shown in Fig. 7, there is no obvious soft phonon mode, indicating that it is very stable.

We have performed optimization of the lattice volume and shape of the ideal structure of FeGe at the DFT level without the Hubbard U correction since the DFT calculation has already correctly produced the ordered magnetic moment of the AFM state measured by the neutron scattering experiment. The optimized lattice parameters are $a = 4.9625$ Å, $c = 4.0667$ Å, which are very close to the experimental values $a = 4.985$ Å, $c = 4.048$ Å. Using the optimized lattice parameters, we have further performed the same calculations for the $2 \times 2 \times 2$ superstructure, as shown in Figs. 2(e) and 2(f). The results are shown in Fig. 8. The CDW state with large dimerization of 1/4 Ge1 sites is still stable, so the slight change of the lattice parameters will not change our conclusion.

As discussed in [61], the lattice instability of FeGe is associated with the B_{1u} soft phonon mode at the L point. However, this soft phonon mode never becomes negative (imaginary) in

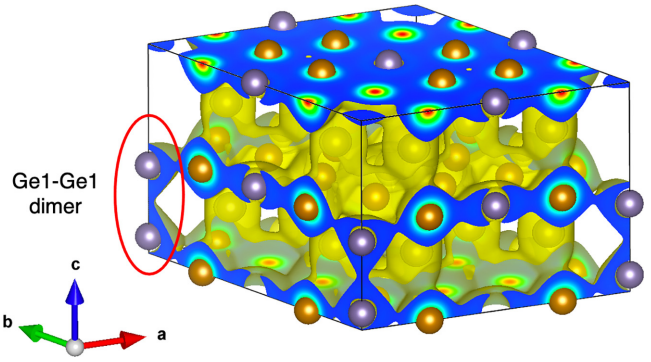

FIG. 6. The charge density map of the $2 \times 2 \times 2$ CDW superstructure of FeGe, calculated by DFT and plotted by VESTA [58]. The red ellipse marks the Ge1-Ge1 dimer.

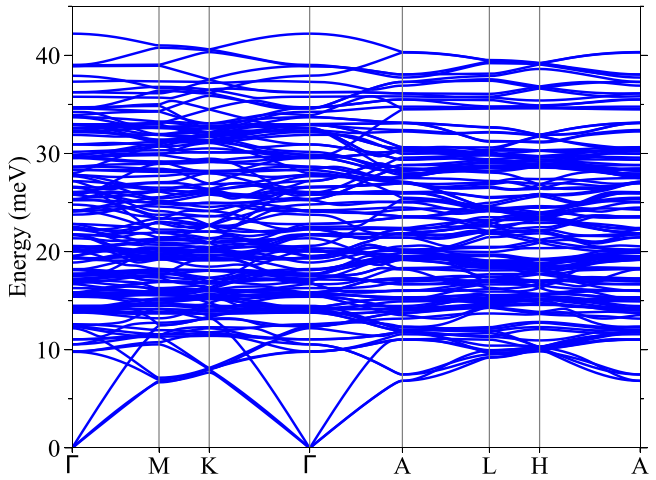

FIG. 7. The calculated phonon spectra for the distorted 2 × 2 × 2 CDW superstructure of FeGe by DFT.

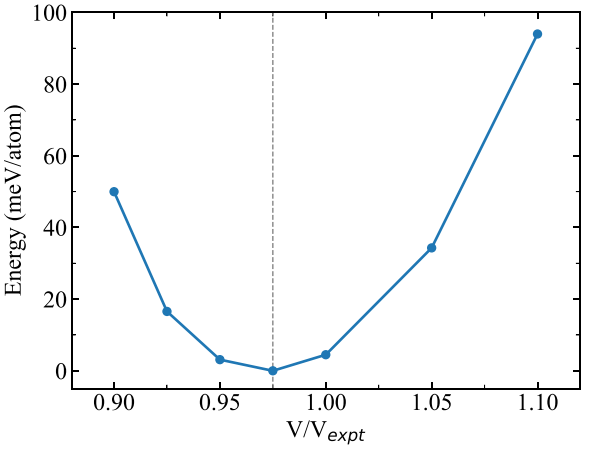

FIG. 9. The total energy vs lattice volume V, calculated by DFT+DMFT for the AFM state of FeGe at $U = 3.9$ eV, $J_H = 0.85$ eV, with the nominal double-counting scheme. V_{expt} is the experimental lattice volume. The calculated equilibrium volume is about $0.975V_{\text{expt}}$.

FeGe, which seems to be in contrast to the soft-mode theory. Actually, for a first-order structural transition, the phonon spectra can be harmonically stable even at $T = 0$ K, which was discussed by Krumhansl and Gooding in Ref. [89]. The famous example is the ω phase in Zr and its alloys. For first-order transitions, the "phonon" concept loses meaning because of a large finite jump and anharmonicity in the order parameters. As we showed in Figs. 2 and 3, and also by x-ray [61] and neutron scattering [59] experiments, the structural transition in FeGe is first order in nature, so we would not expect an imaginary phonon mode; even the distorted structure has lower energy than the ideal structure.

It is known that the double-counting issue of DFT+DMFT may cause trouble in structural optimization in DFT+DMFT calculations, and a different double-counting scheme may lead to different lattice volume. It is possible that the nominal double counting may overestimate the lattice volume in some circumstances. To check how the nominal double-counting scheme affects the lattice volume of FeGe, we have computed the equilibrium volume of FeGe within DFT+DMFT for the AFM state with the same setup, i.e., $U = 3.9$ eV, $J_H = 0.85$ eV, with the nominal double-counting scheme. The result is shown in Fig. 9. It turns out that the calculated equilibrium volume of FeGe (about $0.975V_{\text{expt}}$) is very close to the experimental value (V_{expt}), indicating that the nominal double-counting scheme is a very good choice for the DFT+DMFT calculations for FeGe.

APPENDIX C: DFT RESULTS FOR FeSn

It is noted that the electronic band structures and magnetic orders of FeGe are very similar to its sister compound FeSn, but no CDW has been observed experimentally in FeSn. We also perform DFT calculations for FeSn with the experimental lattice parameters $a = 5.2765$ Å and $c = 4.4443$ Å [74]. The results of the 2 × 2 × 2 superstructure are shown in Fig. 10(a). The DFT method yields an ordered magnetic moment of about 1.94 μ_B/Fe at $d = 0$, which is also close to the value (∼1.85 μ_B/Fe) from the neutron scattering experiment [90]. Therefore, the DFT calculation without Hubbard U is also applicable to the AFM states of FeSn. Although we also find similar behavior of enhanced spin-polarization via large partial Sn1-dimerization in FeSn, the local energy minimum around $d = 1.5$ Å is 5 meV/atom higher than that at $d = 0$ and is far from becoming a true global minimum, consistent with the experiments. Further DFT+U calculations show that it becomes a global minimum only at large U (>2.2 eV),

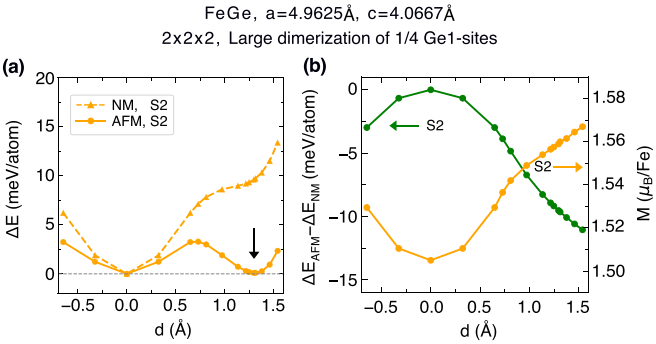

FIG. 8. Analogous to Figs. 2(e) and 2(f), but calculated with the lattice parameters optimized by DFT.

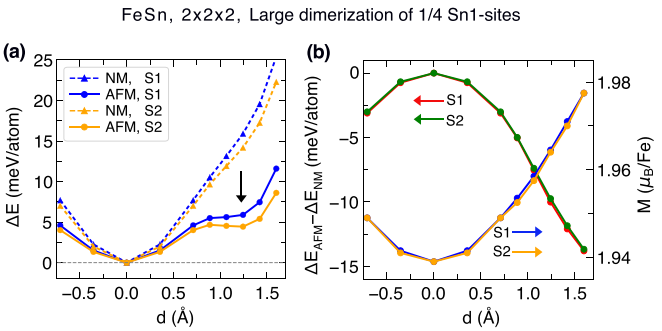

FIG. 10. Analogous to Fig. 2, but calculated by DFT for FeSn with experimental lattice parameters $a = 5.2765$ Å, $c = 4.4443$ Å.

but that will yield a very large ordered magnetic moment of about 2.6 μ_B/Fe, much larger than the experimental value. One possible reason may originate from the fact that Sn has a larger atomic radius than Ge, which also leads to much larger lattice parameters in FeSn than FeGe, i.e., 5.8% larger in a and 9.8% larger in c. The larger atomic radius of Sn and larger crystal volume may cause it to have to pay for more structural distortion energy by dimerizing Sn1 sites, such that the magnetic energy saving never wins in FeSn. Indeed, as shown by the dashed curves in Fig. 10(a), ΔE keeps increasing with $|d|$ without slowing down the rate when the dimerization strength d is ∼1.0–1.5 Å, in sharp contrast to FeGe.

[1] G. Grüner, The dynamics of charge-density waves, Rev. Mod. Phys. **60**, 1129 (1988).

[2] G. Grüner, *Density Waves in Solids* (CRC Press, Boca Raton, FL, 2019).

[3] R. E. Peierls, *Quantum Theory of Solids* (Oxford University Press, Oxford, 2001).

[4] W. L. McMillan, Microscopic model of charge-density waves in 2H-$TaSe_2$, Phys. Rev. B **16**, 643 (1977).

[5] C. M. Varma and A. L. Simons, Strong-coupling theory of charge-density-wave transitions, Phys. Rev. Lett. **51**, 138 (1983).

[6] M. D. Johannes and I. I. Mazin, Fermi surface nesting and the origin of charge density waves in metals, Phys. Rev. B **77**, 165135 (2008).

[7] X. Zhu, Y. Cao, J. Zhang, E. W. Plummer, and J. Guo, Classification of charge density waves based on their nature, Proc. Natl. Acad. Sci. **112**, 2367 (2015).

[8] J. M. Tranquada, B. J. Sternlieb, J. D. Axe, Y. Nakamura, and S. Uchida, Evidence for stripe correlations of spins and holes in copper oxide superconductors, Nature (London) **375**, 561 (1995).

[9] J. E. Hoffman, E. W. Hudson, K. M. Lang, V. Madhavan, H. Eisaki, S. Uchida, and J. C. Davis, A four unit cell periodic pattern of quasiparticle states surrounding vortex cores in $Bi_2Sr_2CaCu_2O_{8+\delta}$, Science **295**, 466 (2002).

[10] S. A. Kivelson, I. P. Bindloss, E. Fradkin, V. Oganesyan, J. M. Tranquada, A. Kapitulnik, and C. Howald, How to detect fluctuating stripes in the high-temperature superconductors, Rev. Mod. Phys. **75**, 1201 (2003).

[11] W. D. Wise, M. C. Boyer, K. Chatterjee, T. Kondo, T. Takeuchi, H. Ikuta, Y. Wang, and E. W. Hudson, Charge-density-wave origin of cuprate checkerboard visualized by scanning tunnelling microscopy, Nat. Phys. **4**, 696 (2008).

[12] D. Reznik, Phonon anomalies and dynamic stripes, Phys. C: Superconduct. **481**, 75 (2012).

[13] E. Blackburn, J. Chang, A. H. Said, B. M. Leu, R. Liang, D. A. Bonn, W. N. Hardy, E. M. Forgan, and S. M. Hayden, Inelastic x-ray study of phonon broadening and charge-density wave formation in Ortho-II-ordered $YBa_2Cu_3O_{6.54}$, Phys. Rev. B **88**, 054506 (2013).

[14] R. Comin, A. Frano, M. M. Yee, Y. Yoshida, H. Eisaki, E. Schierle, E. Weschke, R. Sutarto, F. He, A. Soumyanarayanan, Y. He, M. Le Tacon, I. S. Elfimov, J. E. Hoffman, G. A. Sawatzky, B. Keimer, and A. Damascelli, Charge order driven by Fermi-arc instability in $Bi_2Sr_{2-x}La_xCuO_{6+\delta}$, Science **343**, 390 (2014).

[15] M. Le Tacon, A. Bosak, S. M. Souliou, G. Dellea, T. Loew, R. Heid, K.-P. Bohnen, G. Ghiringhelli, M. Krisch, and B. Keimer, Inelastic x-ray scattering in $YBa_2Cu_3O_{6.6}$ reveals giant phonon anomalies and elastic central peak due to charge-density-wave formation, Nat. Phys. **10**, 52 (2014).

[16] K. Fujita, M. H. Hamidian, S. D. Edkins, C. K. Kim, Y. Kohsaka, M. Azuma, M. Takano, H. Takagi, H. Eisaki, S. ichi Uchida, A. Allais, M. J. Lawler, E.-Ah Kim, S. Sachdev, and J. C. S. Davis, Direct phase-sensitive identification of a d-form factor density wave in underdoped cuprates, Proc. Natl. Acad. Sci. **111**, E3026 (2014).

[17] J. M. Tranquada, D. J. Buttrey, V. Sachan, and J. E. Lorenzo, Simultaneous ordering of holes and spins in $La_2NiO_{4.125}$, Phys. Rev. Lett. **73**, 1003 (1994).

[18] S.-H. Lee and S-W. Cheong, Melting of quasi-two-dimensional charge stripes in $La_{5/3}$ $Sr_{1/3}$ NiO_4, Phys. Rev. Lett. **79**, 2514 (1997).

[19] Y.-X. Jiang, J.-X. Yin, M. M. Denner, N. Shumiya, B. R. Ortiz, G. Xu, Z. Guguchia, J. He, Md S. Hossain, X. Liu, J. Ruff, L. Kautzsch, S. S. Zhang, G. Chang, I. Belopolski, Q. Zhang, T. A. Cochran, D. Multer, M. Litskevich, Z.-J. Cheng *et al.*, Unconventional chiral charge order in kagome superconductor KV_3 Sb_5, Nat. Mater. **20**, 1353 (2021).

[20] C. Mielke III, D. Das, J.-X. Yin, H. Liu, R. Gupta, Y.-X. Jiang, M. Medarde, X. Wu, H. C. Lei, J. Chang, P. Dai, Q. Si, H. Miao, R. Thomale, T. Neupert, Y. Shi, R. Khasanov, M. Z. Hasan, H. Luetkens, and Z. Guguchia, Time-reversal symmetry-breaking charge order in a kagome superconductor, Nature (London) **602**, 245 (2022).

[21] B. R. Ortiz, L. C. Gomes, J. R. Morey, M. Winiarski, M. Bordelon, J. S. Mangum, I. W. H. Oswald, J. A. Rodriguez-Rivera, J. R. Neilson, S. D. Wilson, E. Ertekin, T. M. McQueen, and E. S. Toberer, New kagome prototype materials: Discovery of KV_3Sb_5, RbV_3Sb_5 and CsV_3Sb_5, Phys. Rev. Mater. **3**, 094407 (2019).

[22] B. R. Ortiz, S. M. L. Teicher, Y. Hu, J. L. Zuo, P. M. Sarte, E. C. Schueller, A. M. M. Abeykoon, M. J. Krogstad, S. Rosenkranz, R. Osborn, R. Seshadri, L. Balents, J. He, and S. D. Wilson, CsV_3 Sb_5: A Z_2 topological kagome metal with a superconducting ground state, Phys. Rev. Lett. **125**, 247002 (2020).

[23] S.-Y. Yang, Y. Wang, B. R. Ortiz, D. Liu, J. Gayles, E. Derunova, R. Gonzalez-Hernandez, L. Å mejkal, Y. Chen, S. S. P. Parkin, S. D. Wilson, E. S. Toberer, T. McQueen, and M. N. Ali, Giant, unconventional anomalous Hall effect in the metallic frustrated magnet candidate, KV_3Sb_5, Sci. Adv. **6**, eabb6003 (2020).

[24] X. Feng, K. Jiang, Z. Wang, and J. Hu, Chiral flux phase in the kagome superconductor AV_3Sb_5, Sci. Bull. **66**, 1384 (2021).

[25] M. L. Kiesel, C. Platt, and R. Thomale, Unconventional Fermi surface instabilities in the kagome Hubbard model, Phys. Rev. Lett. **110**, 126405 (2013).

[26] W.-S. Wang, Z.-Z. Li, Y.-Y. Xiang, and Q.-H. Wang, Competing electronic orders on kagome lattices at van Hove filling, Phys. Rev. B **87**, 115135 (2013).

[27] H. Tan, Y. Liu, Z. Wang, and B. Yan, Charge density waves and electronic properties of superconducting kagome metals, Phys. Rev. Lett. **127**, 046401 (2021).

[28] H. Li, T. T. Zhang, T. Yilmaz, Y. Y. Pai, C. E. Marvinney, A. Said, Q. W. Yin, C. S. Gong, Z. J. Tu, E. Vescovo, C. S. Nelson, R. G. Moore, S. Murakami, H. C. Lei, H. N. Lee, B. J. Lawrie, and H. Miao, Observation of unconventional charge density wave without acoustic phonon anomaly in kagome superconductors AV_3Sb_5 (A=Rb, Cs), Phys. Rev. X **11**, 031050 (2021).

[29] M. M. Denner, R. Thomale, and T. Neupert, Analysis of charge order in the kagome metal AV_3Sb_5 (A=K, Rb, Cs), Phys. Rev. Lett. **127**, 217601 (2021).

[30] Y.-P. Lin and R. M. Nandkishore, Complex charge density waves at van Hove singularity on hexagonal lattices: Haldane-model phase diagram and potential realization in the kagome metals AV_3 Sb_5 (A=K, Rb, Cs), Phys. Rev. B **104**, 045122 (2021).

[31] T. Park, M. Ye, and L. Balents, Electronic instabilities of kagome metals: Saddle points and Landau theory, Phys. Rev. B **104**, 035142 (2021).

[32] M. H. Christensen, T. Birol, B. M. Andersen, and R. M. Fernandes, Theory of the charge density wave in AV_3Sb_5 kagome metals, Phys. Rev. B **104**, 214513 (2021).

[33] H. Zhao, H. Li, B. R. Ortiz, S. M. L. Teicher, T. Park, M. Ye, Z. Wang, L. Balents, S. D. Wilson, and I. Zeljkovic, Cascade of correlated electron states in the kagome superconductor CsV_3Sb_5, Nature (London) **599**, 216 (2021).

[34] K. Jiang, T. Wu, J.-X. Yin, Z. Wang, M. Z. Hasan, S. D Wilson, X. Chen, and J. Hu, Kagome superconductors AV_3Sb_5 (A=K, Rb, Cs), Natl. Sci. Rev. **10**, nwac199 (2022).

[35] L. Nie, K. Sun, W. Ma, D. Song, L. Zheng, Z. Liang, P. Wu, F. Yu, J. Li, M. Shan, D. Zhao, S. Li, B. Kang, Z. Wu, Y. Zhou, K. Liu, Z. Xiang, J. Ying, Z. Wang, T. Wu *et al.*, Charge-density-wave-driven electronic nematicity in a kagome superconductor, Nature (London) **604**, 59 (2022).

[36] I. Syôzi, Statistics of kagomeé lattice, Prog. Theor. Phys. **6**, 306 (1951).

[37] S. Sachdev, Kagome- and triangular-lattice Heisenberg antiferromagnets: Ordering from quantum fluctuations and quantum-disordered ground states with unconfined bosonic spinons, Phys. Rev. B **45**, 12377 (1992).

[38] M. R. Norman, Colloquium: Herbertsmithite and the search for the quantum spin liquid, Rev. Mod. Phys. **88**, 041002 (2016).

[39] E. Tang, J.-W. Mei, and X.-G. Wen, High-temperature fractional quantum Hall states, Phys. Rev. Lett. **106**, 236802 (2011).

[40] J.-X. Yin, S. S. Zhang, H. Li, K. Jiang, G. Chang, B. Zhang, B. Lian, C. Xiang, I. Belopolski, H. Zheng, T. A. Cochran, S.-Y. Xu, G. Bian, K. Liu, T.-R. Chang, H. Lin, Z.-Y. Lu, Z. Wang, S. Jia, W. Wang *et al.*, Giant and anisotropic many-body spin–orbit tunability in a strongly correlated kagome magnet, Nature (London) **562**, 91 (2018).

[41] J.-X. Yin, N. Shumiya, S. Mardanya, Q. Wang, S. S. Zhang, H.-J. Tien, D. Multer, Y. Jiang, G. Cheng, N. Yao, S. Wu, D. Wu, L. Deng, Z. Ye, R. He, G. Chang, Z. Liu, K. Jiang, Z. Wang, T. Neupert *et al.*, Fermion–boson many-body interplay in a frustrated kagome paramagnet, Nat. Commun. **11**, 4003 (2020).

[42] Z. Liu, M. Li, Q. Wang, G. Wang, C. Wen, K. Jiang, X. Lu, S. Yan, Y. Huang, D. Shen, J.-X. Yin, Z. Wang, Z. Yin, H. Lei, and S. Wang, Orbital-selective Dirac fermions and extremely flat bands in frustrated kagome-lattice metal CoSn, Nat. Commun. **11**, 4002 (2020).

[43] M. Kang, L. Ye, S. Fang, J.-S. You, A. Levitan, M. Han, J. I. Facio, C. Jozwiak, A. Bostwick, E. Rotenberg, M. K. Chan, R. D. McDonald, D. Graf, K. Kaznatcheev, E. Vescovo, D. C. Bell, E. Kaxiras, J. van den Brink, M. Richter, M. Prasad Ghimire *et al.*, Dirac fermions and flat bands in the ideal kagome metal FeSn, Nat. Mater. **19**, 163 (2020).

[44] Y. Wang, Electronic correlation effects on stabilizing a perfect kagome lattice and ferromagnetic fluctuation in $LaRu_3Si_2$, JUSTC **53**, 0702 (2023).

[45] H. Tasaki, Ferromagnetism in the Hubbard models with degenerate single-electron ground states, Phys. Rev. Lett. **69**, 1608 (1992).

[46] Z. Lin, J.-H. Choi, Q. Zhang, W. Qin, S. Yi, P. Wang, L. Li, Y. Wang, H. Zhang, Z. Sun, L. Wei, S. Zhang, T. Guo, Q. Lu, J.-H. Cho, C. Zeng, and Z. Zhang, Flat bands and emergent ferromagnetic ordering in Fe_3Sn_2 kagome lattices, Phys. Rev. Lett. **121**, 096401 (2018).

[47] J.-X. Yin, S. S. Zhang, G. Chang, Q. Wang, S. S. Tsirkin, Z. Guguchia, B. Lian, H. Zhou, K. Jiang, I. Belopolski, N. Shumiya, D. Multer, M. Litskevich, T. A. Cochran, H. Lin, Z. Wang, T. Neupert, S. Jia, H. Lei, and M. Z. Hasan, Negative flat band magnetism in a spin–orbit-coupled correlated kagome magnet, Nat. Phys. **15**, 443 (2019).

[48] J.-X. Yin, W. Ma, T. A. Cochran, X. Xu, S. S. Zhang, H.-J. Tien, N. Shumiya, G. Cheng, K. Jiang, B. Lian, Z. Song, G. Chang, I. Belopolski, D. Multer, M. Litskevich, Z.-J. Cheng, X. P. Yang, B. Swidler, H. Zhou, H. Lin *et al.*, Quantum-limit Chern topological magnetism in $TbMn_6Sn_6$, Nature (London) **583**, 533 (2020).

[49] J. Zhang, T. Yilmaz, J. W. R. Meier, J. Y. Pai, J. Lapano, H. X. Li, K. Kaznatcheev, E. Vescovo, A. Huon, M. Brahlek, T. Z. Ward, B. Lawrie, R. G. Moore, H. N. Lee, Y. L. Wang, H. Miao, and B. Sales, Flat band induced negative magnetoresistance in multi-orbital kagome metal, arXiv:2105.08888.

[50] H. Huang, L. Zheng, Z. Lin, X. Guo, S. Wang, S. Zhang, C. Zhang, Z. Sun, Z. Wang, H. Weng, L. Li, T. Wu, X. Chen, and C. Zeng, Flat-band-induced anomalous anisotropic charge transport and orbital magnetism in kagome metal CoSn, Phys. Rev. Lett. **128**, 096601 (2022).

[51] L. Ye, M. Kang, J. Liu, F. von Cube, C. R. Wicker, T. Suzuki, C. Jozwiak, A. Bostwick, E. Rotenberg, D. C. Bell, L. Fu, R. Comin, and J. G. Checkelsky, Massive Dirac fermions in a ferromagnetic kagome metal, Nature (London) **555**, 638 (2018).

[52] Z. Liang, X. Hou, F. Zhang, W. Ma, P. Wu, Z. Zhang, F. Yu, J.-J. Ying, K. Jiang, L. Shan, Z. Wang, and X.-H. Chen, Three-dimensional charge density wave and surface-dependent vortex-core states in a kagome superconductor CsV_3Sb_5, Phys. Rev. X **11**, 031026 (2021).

[53] S. Zhou and Z. Wang, Chern Fermi pocket, topological pair density wave, and charge-4e and charge-6e superconductivity in kagome superconductors, Nat. Commun. **13**, 7288 (2022).

[54] Z. Ye, A. Luo, J.-X. Yin, M. Z. Hasan, and G. Xu, Structural instability and charge modulations in the kagome superconductor AV_3Sb_5, Phys. Rev. B **105**, 245121 (2022).

[55] Y. Xie, Y. Li, P. Bourges, A. Ivanov, Z. Ye, J.-X. Yin, M. Z. Hasan, A. Luo, Y. Yao, Z. Wang, G. Xu, and P. Dai, Electron-phonon coupling in the charge density wave state of CsV_3Sb_5, Phys. Rev. B **105**, L140501 (2022).

[56] G. Liu, X. Ma, K. He, Q. Li, H. Tan, Y. Liu, J. Xu, W. Tang, K. Watanabe, T. Taniguchi, L. Gao, Y. Dai, H.-H. Wen, B. Yan, and X. Xi, Observation of anomalous amplitude modes in the kagome metal CsV_3Sb_5, Nat. Commun. **13**, 3461 (2022).

[57] Y. Zhong, S. Li, H. Liu, Y. Dong, K. Aido, Y. Arai, H. Li, W. Zhang, Y. Shi, Z. Wang, S. Shin, H. N. Lee, H. Miao, T. Kondo, and K. Okazaki, Testing electron-phonon coupling for the superconductivity in kagome metal CsV_3Sb_5, Nat. Commun. **14**, 1945 (2023).

[58] K. Momma and F. Izumi, VESTA: A three-dimensional visualization system for electronic and structural analysis, J. Appl. Crystallogr. **41**, 653 (2008).

[59] X. Teng, L. Chen, F. Ye, E. Rosenberg, Z. Liu, J.-X. Yin, Y.-X. Jiang, J. S. Oh, M. Z. Hasan, K. J. Neubauer, B. Gao, Y. Xie, M. Hashimoto, D. Lu, C. Jozwiak, A. Bostwick, E. Rotenberg, R. J. Birgeneau, J.-H. Chu, M. Yi *et al.*, Discovery of charge density wave in a kagome lattice antiferromagnet, Nature (London) **609**, 490 (2022).

[60] J.-X. Yin, Y.-X. Jiang, X. Teng, M. S. Hossain, S. Mardanya, T.-R. Chang, Z. Ye, G. Xu, M. M. Denner, T. Neupert, B. Lienhard, H.-B. Deng, C. Setty, Q. Si, G. Chang, Z. Guguchia, B. Gao, N. Shumiya, Q. Zhang, T. A. Cochran *et al.*, Discovery of charge order and corresponding edge state in kagome magnet FeGe, Phys. Rev. Lett. **129**, 166401 (2022).

[61] H. Miao, T. T. Zhang, H. X. Li, G. Fabbris, A. H. Said, R. Tartaglia, T. Yilmaz, E. Vescovo, J.-X. Yin, S. Murakami, X. L. Feng, K. Jiang, X. L. Wu, A. F. Wang, S. Okamoto, Y. L. Wang, and H. N. Lee, Signature of spin-phonon coupling driven charge density wave in a kagome magnet, Nat. Commun. **14**, 6183 (2023).

[62] F. H. Yu, T. Wu, Z. Y. Wang, B. Lei, W. Z. Zhuo, J. J. Ying, and X. H. Chen, Concurrence of anomalous Hall effect and charge density wave in a superconducting topological kagome metal, Phys. Rev. B **104**, L041103 (2021).

[63] X. Teng, J. S. Oh, H. Tan, L. Chen, J. Huang, B. Gao, J.-X. Yin, J.-H. Chu, M. Hashimoto, D. Lu, C. Jozwiak, A. Bostwick, E. Rotenberg, G. E. Granroth, B. Yan, R. J. Birgeneau, P. Dai, and M. Yi, Magnetism and charge density wave order in kagome FeGe, Nat. Phys. **19**, 814 (2023).

[64] C. Setty, C. A. Lane, L. Chen, H. Hu, J.-X. Zhu, and Q. Si, Electron correlations and charge density wave in the topological kagome metal FeGe, arXiv:2203.01930.

[65] S. Shao, J.-X. Yin, I. Belopolski, J.-Y. You, T. Hou, H. Chen, Y. Jiang, Md S. Hossain, M. Yahyavi, C.-H. Hsu, Y. P. Feng, A. Bansil, M. Z. Hasan, and G. Chang, Intertwining of magnetism and charge ordering in kagome FeGe, ACS Nano **17**, 10164 (2023).

[66] H. Zhou, S. Yan, D. Fan, D. Wang, and X. Wan, Magnetic interactions and possible structural distortion in kagome FeGe from first-principles study and symmetry analysis, Phys. Rev. B **108**, 035138 (2023).

[67] L. Wu, Y. Hu, D. Wang, and X. Wan, Novel three-dimensional Fermi surface and electron-correlation-induced charge density wave in FeGe, arXiv:2302.03622.

[68] H.-Y. Ma, J.-X. Yin, M. Z. Hasan, and J. Liu, Theory for charge density wave and orbital-flux state in antiferromagnetic kagome metal FeGe, arXiv:2303.02824.

[69] A. I. Lichtenstein, M. I. Katsnelson, and G. Kotliar, Finite-temperature magnetism of transition metals: An *ab initio* dynamical mean-field theory, Phys. Rev. Lett. **87**, 067205 (2001).

[70] G. Kotliar, S. Y. Savrasov, K. Haule, V. S. Oudovenko, O. Parcollet, and C. A. Marianetti, Electronic structure calculations with dynamical mean-field theory, Rev. Mod. Phys. **78**, 865 (2006).

[71] G. Kresse and J. Furthmüller, Efficient iterative schemes for *ab initio* total-energy calculations using a plane-wave basis set, Phys. Rev. B **54**, 11169 (1996).

[72] P. E. Blöchl, Projector augmented-wave method, Phys. Rev. B **50**, 17953 (1994).

[73] J. P. Perdew, K. Burke, and M. Ernzerhof, Generalized gradient approximation made simple, Phys. Rev. Lett. **77**, 3865 (1996).

[74] W. R. Meier, M.-H. Du, S. Okamoto, N. Mohanta, A. F. May, M. A. McGuire, C. A. Bridges, G. D. Samolyuk, and B. C. Sales, Flat bands in the CoSn-type compounds, Phys. Rev. B **102**, 075148 (2020).

[75] K. Haule, C.-H. Yee, and K. Kim, Dynamical mean-field theory within the full-potential methods: Electronic structure of $CeIrIn_5$, $CeCoIn_5$, and $CeRhIn_5$, Phys. Rev. B **81**, 195107 (2010).

[76] K. Haule and T. Birol, Free energy from stationary implementation of the DFT + DMFT functional, Phys. Rev. Lett. **115**, 256402 (2015).

[77] P. Blaha, K. Schwarz, F. Tran, R. Laskowski, G. K. H. Madsen, and L. D. Marks, WIEN2k: An APW+lo program for calculating the properties of solids, J. Chem. Phys. **152**, 074101 (2020).

[78] S. A. Herrera and G. G. Naumis, Electronic and optical conductivity of Kekulé-patterned graphene: Intravalley and intervalley transport, Phys. Rev. B **101**, 205413 (2020).

[79] Z. Chen, X. Wu, R. Yin, J. Zhang, S. Wang, Y. Li, M. Li, A. Wang, Y. Wang, Y.-J. Yan, and D.-L. Feng, Charge density wave with strong quantum phase fluctuations in kagome magnet FeGe, arXiv:2302.04490.

[80] L. Huang and H. Lu, Signatures of Hundness in kagome metals, Phys. Rev. B **102**, 125130 (2020).

[81] Z. P. Yin, K. Haule, and G. Kotliar, Kinetic frustration and the nature of the magnetic and paramagnetic states in iron pnictides and iron chalcogenides, Nat. Mater. **10**, 932 (2011).

[82] E. Ieki, K. Nakayama, Y. Miyata, T. Sato, H. Miao, N. Xu, X.-P. Wang, P. Zhang, T. Qian, P. Richard, Z.-J. Xu, J. S. Wen, G. D. Gu, H. Q. Luo, H.-H. Wen, H. Ding, and T. Takahashi, Evolution from incoherent to coherent electronic states and its implications for superconductivity in $FeTe_{1-x}Se_x$, Phys. Rev. B **89**, 140506(R) (2014).

[83] K. Haule and G. L. Pascut, Forces for structural optimizations in correlated materials within a DFT+embedded DMFT functional approach, Phys. Rev. B **94**, 195146 (2016).

[84] Z. Chen, X. Wu, S. Zhou, J. Zhang, R. Yin, Y. Li, M. Li, J. Gong, M. He, Y. Chai, X. Zhou, Y. Wang, A. Wang, Y.-J. Yan, and D.-L. Feng, Long-ranged charge order conspired by

magnetism and lattice in an antiferromagnetic kagome metal, arXiv:2307.07990.

[85] Z. Zhao, T. Li, P. Li, X. Wu, J. Yao, Z. Chen, S. Cui, Z. Sun, Y. Yang, Z. Jiang, Z. Liu, A. Louat, T. Kim, C. Cacho, A. Wang, Y. Wang, D. Shen, J. Jiang, and D. Feng, Photoemission evidence of a novel charge order in kagome metal FeGe, arXiv:2308.08336.

[86] S. L. Dudarev, G. A. Botton, S. Y. Savrasov, C. J. Humphreys, and A. P. Sutton, Electron-energy-loss spectra and the structural stability of nickel oxide: An LSDA+U study, Phys. Rev. B **57**, 1505 (1998).

[87] E. Gull, A. J. Millis, A. I. Lichtenstein, A. N. Rubtsov, M. Troyer, and P. Werner, Continuous-time Monte Carlo methods for quantum impurity models, Rev. Mod. Phys. **83**, 349 (2011).

[88] http://hauleweb.rutgers.edu/tutorials/Tutorial1a.html.

[89] J. A. Krumhansl and R. J. Gooding, Structural phase transitions with little phonon softening and first-order character, Phys. Rev. B **39**, 3047 (1989).

[90] B. C. Sales, J. Yan, W. R. Meier, A. D. Christianson, S. Okamoto, and M. A. McGuire, Electronic, magnetic, and thermodynamic properties of the kagome layer compound FeSn, Phys. Rev. Mater. **3**, 114203 (2019).